PHILOSOPHICAL TRANSACTIONS A

royalsocietypublishing.org/journal/rsta

Research

Cite this article: Gaikwad HK, Jaswandkar SV, Katti KS, Haage A, Katti DR. 2023 Molecular basis of conformational changes and mechanics of integrins. *Phil. Trans. R. Soc. A* **381**: 20220243.
https://doi.org/10.1098/rsta.2022.0243

Received: 8 October 2022
Accepted: 13 January 2023

One contribution of 13 to a discussion meeting issue 'Supercomputing simulations of advanced materials'.

Subject Areas:
computational biology, computational mechanics, computer modelling and simulation, biomedical engineering, materials science

Keywords:
integrins, molecular dynamics, mechanics, mechanical properties, folding, unfolding

Author for correspondence:
Dinesh R. Katti
e-mail: dinesh.katti@ndsu.edu

Electronic supplementary material is available online at https://doi.org/10.6084/m9.figshare.c.6494013.

THE ROYAL SOCIETY PUBLISHING

Molecular basis of conformational changes and mechanics of integrins

Hanmant K. Gaikwad[1], Sharad V. Jaswandkar[1], Kalpana S. Katti[1], Amanda Haage[2] and Dinesh R. Katti[1]

[1]Department of Civil, Construction and Environmental Engineering, North Dakota State University, Fargo, ND 58105, USA
[2]Department of Biomedical Sciences, University of North Dakota, Grand Forks, ND 58202, USA

HKG, 0000-0001-9078-8038; SVJ, 0000-0003-3959-0071; KSK, 0000-0002-1404-4018; AH, 0000-0001-6305-440X; DRK, 0000-0001-9866-2683

Integrin, as a mechanotransducer, establishes the mechanical reciprocity between the extracellular matrix (ECM) and cells at integrin-mediated adhesion sites. This study used steered molecular dynamics (SMD) simulations to investigate the mechanical responses of integrin $\alpha_V\beta_3$ with and without 10th type III fibronectin ($FnIII_{10}$) binding for tensile, bending and torsional loading conditions. The ligand-binding integrin confirmed the integrin activation during equilibration and altered the integrin dynamics by changing the interface interaction between β-tail, hybrid and epidermal growth factor domains during initial tensile loading. The tensile deformation in integrin molecules indicated that fibronectin ligand binding modulates its mechanical responses in the folded and unfolded conformation states. The bending deformation responses of extended integrin models reveal the change in behaviour of integrin molecules in the presence of Mn^{2+} ion and ligand based on the application of force in the folding and unfolding directions of integrin. Furthermore, these SMD simulation results were used to predict the mechanical properties of integrin underlying the mechanism of integrin-based adhesion. The evaluation of integrin mechanics provides new insights into understanding the mechanotransmission (force transmission) between cells and ECM and contributes to developing an accurate model for integrin-mediated adhesion.

This article is part of a discussion meeting issue 'Supercomputing simulations of advanced materials'.

royalsocietypublishing.org/journal/rsta Phil. Trans. R. Soc. A 381: 20220243

1. Introduction

Integrins are heterodimeric transmembrane adhesion proteins that couple the extracellular matrix (ECM) to the cell cytoskeleton and facilitate cell migration, proliferation and differentiation [1,2]. They are composed of 18 α and eight β subunits, which assemble non-covalently into 24 different heterodimers in mammals [3–7]. The integrin ectodomain, including $\alpha_v\beta_3$, studied here, consists of two subunits, where the head of the subunits is supported by the two legs (figure 1*a*) [1]. The head of the integrin $\alpha_v\beta_3$ consists of the β-propeller domain of the α_v subunit and the βA (or βI) domain of β_3 subunits. The two long legs contain thigh, calf-1, and calf-2 domains of the α_v subunit and the hybrid, plexin/semaphorin/integrin (PSI), epidermal growth factor (EGF) 1–4 domains and the β tail domain (βTD) of the β_3 subunit (figure 1*a*). The integrin domains are distinguished into three main regions: the extracellular domain outside the cell, the transmembrane portion that pierces the cell membrane and the cytoplasmic tails inside the cell [8]. Under physiological conditions, integrins may adopt an inactive state with low affinities for ligands. In response to extracellular or intracellular stimuli, they may alter their conformations, bind ligands with high affinities and transmit signals across the plasma membrane [1]. In the deactivated state, ectodomains of α and β subunits are in folded shape laterally associated with transmembrane and cytoplasmic domains. Upon integrin activation, the distal portions of both ectodomains swing out like a switchblade, causing the transmembrane and cytoplasmic domains to separate [9]. In outside-in signalling, ligand binding to the ectodomain has induced the integrin activation and opened the hinge angle between the βA and hybrid domains at integrin headpiece regions [10,11]. Switching to high binding affinity has been associated with the opening of this hinge [12,13]. During inside-out signalling, talin binds to the cytoplasmic tail α and β subunit, causing the tail separation and increasing the affinity of integrin ectodomain for ECM ligand [14]. Activation and deactivation of the integrin affect the ability of cell adhesion with binding affinity for ECM ligands [15] and change the mechanics of the cell [1]. Ligand-induced structural changes linked to filamentous actin, focal adhesion proteins and integrin cytoplasmic tails result in cell spreading. The disruption of these processes contributes to the pathogenesis of many diseases [16,17]. The over-expression of integrin $\alpha_v\beta_3$ in certain tumour cells alters the cell mechanics and encourages tumour development, angiogenesis and metastasis [18,19]. The integrins serve essential roles in the process associated with cancer progression, including invasion, migration, proliferation and survival [20].

Integrins are considered essential for transmitting and sensing the mechanical forces in focal adhesion and translating the force into biochemical signals as mechanotransducers [21]. As transmembrane mechanical links between intracellular and extracellular sites [1], integrins frequently experience tensile forces internally at the cytoplasmic tail, where the cytoskeleton is attached, or externally at the head, where ligands bind. Therefore, a pulling force could straighten a folded integrin and even bring about other conformational alterations that activate the integrin and strengthen the integrin-mediated adhesion [16]. However, the transmission of force through the molecule and molecular mechanisms that control the assembly of integrin clustering to form focal adhesion is poorly understood. Prior experimental studies used several advanced techniques to investigate force transduction during integrin-mediated adhesion. Forster resonance energy transfer (FRET) [22], optical tweezers [23], atomic force microscopy (AFM) [24] and the biomembrane force probe (BFP) [25] are commonly used techniques for single molecule force measurement. In living cells at the integrin-engaged fibronectin synergy site, FRET-based molecular tension sensors were used to measure the distribution of loads experienced by individual integrins. The dynamics of the integrin-mediated adhesion were characterized by the BFP technique, which has demonstrated the role of mechanical force in

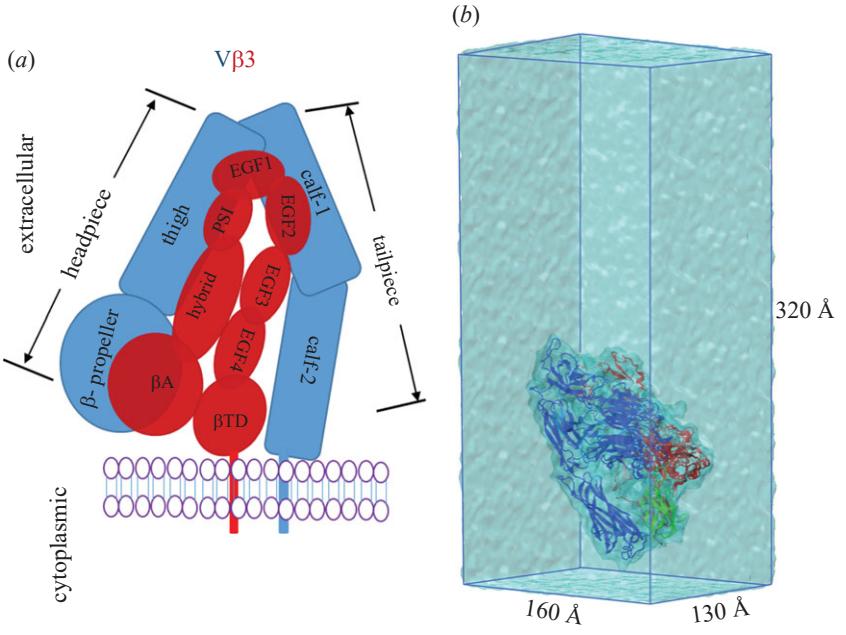

Figure 1. System set-up (*a*) schematic of an extracellular portion of integrin $\alpha_v\beta_3$ showing the various domains of the α_v (blue) and β_3 (red) subunits (*b*) solvated structure of IVB used for all IVD simulation with integrin subunits α_v (blue) and β_3 (red), attached with $FnIII_{10}$ ligand (green). Box with cyan colour represents the solvated water box. The same colour scheme and representation are used for all the figures.

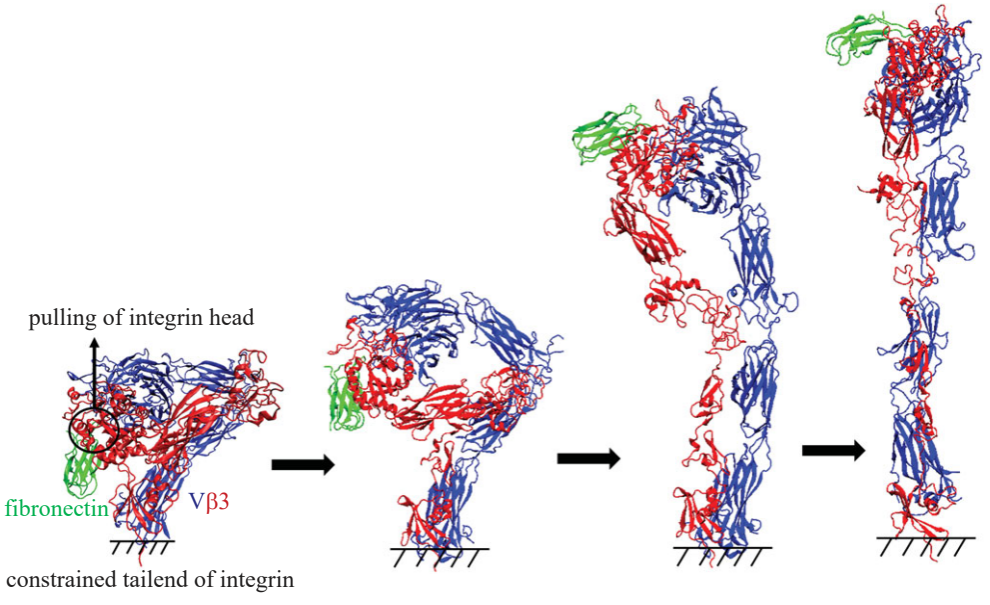

Figure 2. Forced-induced tensile deformation of integrin $\alpha_v\beta_3$: illustration of forced-induced tensile deformation and snapshots of the unfolding process of integrin IV3 with constant velocity 0.01 Å/ps until fully extended, where constraints applied at βTD and head domains βA and β-propeller were pulled for tensile deformation. Here, the integrin molecule rotated around the genu and moved in a pulling direction without detachment from the $FnIII_{10}$ ligand.

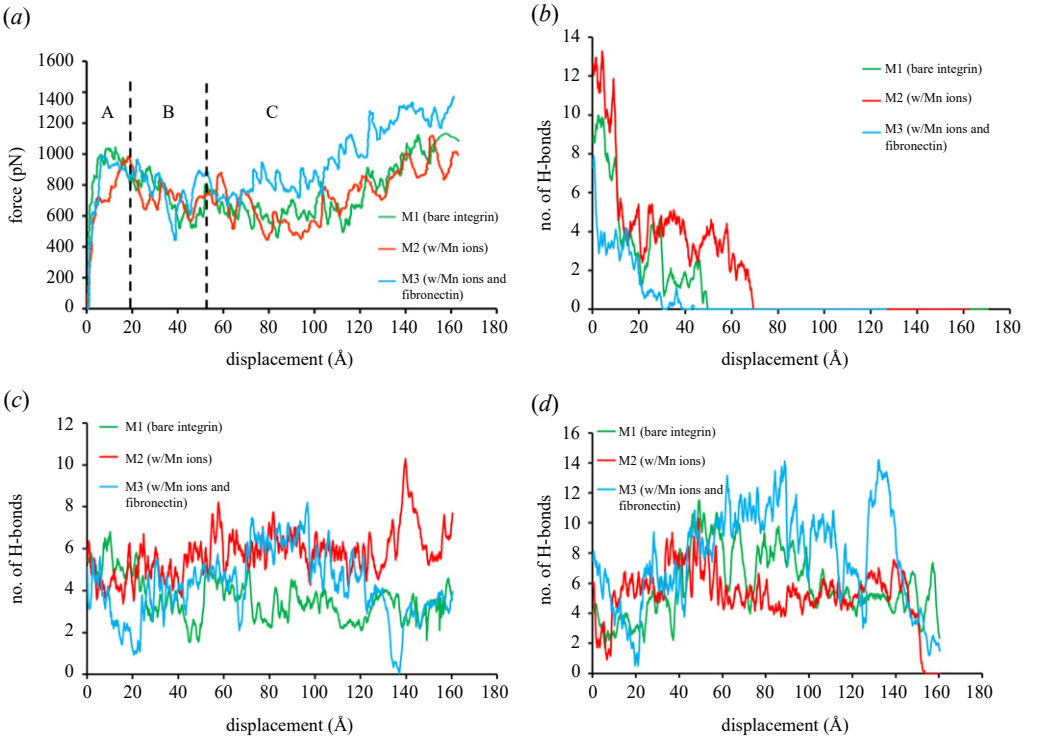

Figure 3. The tensile deformation responses and hydrogen bond analysis. (*a*) The force–displacement responses of all integrin models (M1, M2 and M3) for 0.01 Å/ps pulling speed divides into three regimes: A-Pre-relaxation stiffening at in, B-Force relaxation and C-Post-relaxation stiffening. (*b*) The breaking of hydrogen bonds between the head domains (hybrid and βA) and the tail domains (βTD, EGF-3 and EGF-4) finally resulted in the detachment of the headpiece and tailpiece domains. (*c*) The formation of hydrogen bonds between genu domains (Calf-1, and EGF-1, EGF-2) during force relaxation and beginning of post-relaxation exerted the more force for the deformation in the post-relaxation region. (*d*) The decrement in the hydrogen bonds in the initial and final phase of the deformation execute the separation of tail domains (βTD and Calf-2).

regulating the conformational changes in integrin $\alpha_v\beta_3$ activation [25]. AFM has also measured the binding forces between integrin and some ligands. It has been observed that ligand binding affinity changed as the integrin bound with different ligands [26,27]. The affinity of the integrin headpiece for ligand is also influenced by divalent cations, typically Mn^{2+} and Mg^{2+}, promoting the binding and Ca^{2+} inhibiting it [28–30]. Besides experimental studies, computational approaches have been applied to provide insights into the structural mechanism of integrin during cellular mechanosensing. The molecular dynamics (MD) simulation study demonstrated the integrin activation of liganded integrin $\alpha_v\beta_3$ structure by opening βA and hybrid domains [31]. Force-induced unbending of integrin through steered MD (SMD) revealed the dynamics and pathways of integrin activation in atomic details [32]. SMD simulation was conducted on the extended model of the entire ectodomain of integrin $\alpha_{IIb}\beta_3$ to evaluate the conformational change between the closed and open legs [33]. In prior studies, the structural behaviour of integrin is not investigated for the mechanical properties at the atomic level. In this study, SMD simulations are performed to predict the mechanical behaviour of integrin for force induce activation. The mechanical properties of integrin are evaluated in a manner similar to that used in the protein-based deformational behaviour studies on actin and collagen [34,35]. Here, the mechanical deformation of integrin has been investigated for tension, bending and torsional loading conditions. These are some conceivable loading paths an integrin molecule may be subjected to. Also, integrin dynamics have been analysed after considering the effect of metal ion Mn^{2+} and fibronectin binding on integrin-mediated adhesion.

royalsocietypublishing.org/journal/rsta Phil. Trans. R. Soc. A 381: 20220243

2. Results and discussion

In the present work, the mechanical responses of integrin molecules were tested for different integrin environment conditions. Therefore, the three integrin models were prepared based on ligand attachment and the presence of metal ions, denoted as model M1 (integrin molecule $\alpha_v\beta_3$ in the absence of Mn^{2+} ion, and ligand (10th type III fibronectin($FnIII_{10}$)), model M2 (integrin molecule $\alpha_v\beta_3$ in the presence of Mn^{2+} ion without ligand attachment) and model M3 (integrin molecule $\alpha_v\beta_3$ in the presence of Mn^{2+} ion with ligand attachment). In the subsequent section, these models are mentioned as M1, M2 and M3.

(a) Tensile deformation of integrin

The transformation of integrin from folding to unfolding state induced tensile forces on the integrin molecule during the transmission of forces between ECM & Cytoskeleton. In tensile loading, this deformational behaviour of integrin molecules has been investigated for the force-induced unfolding of integrin using the SMD approach. To perform the tensile loading simulation, the βTD was fixed, and head domains βA and β-propeller were pulled for different constant velocities (figure 2).

This simulation evaluated the mechanical behaviour of the integrin molecule to find structural stiffness based on force-displacement response. As shown in figure 3*a*, the force responses for all the models showed similar deformation behaviour, divided into three regions: A-Pre-relaxation stiffening, B-Force relaxation and C-Post-relaxation stiffening. The pre-relaxation stiffening is observed in the initial stage of pulling up to 10 Å deformation, followed by force relaxation for 50 Å. The post-relaxation stiffening begins after the force has relaxed and continues until the integrin models have fully extended. The deformation responses for different velocities also showed similar deformational behaviour for all integrin models, and a higher magnitude of force for a given deformation has been observed at higher velocities (electronic supplementary material, figures S1.3*a*, S1.4*a*, S1.5*a*). The influence of strain rate-based deformation on the application of force for the molecule has been reported in prior molecular dynamic studies for integrin and other protein molecules [32,34].

The resistance to the unfolding defines the stiffness of the integrin molecule and has been evaluated by the given expression, $K = F/\delta$, where K is the stiffness of the integrin molecule, and F is the applied force for the given deformation (δ) [35]. From the pre-relaxation region, the first linear regime of force–displacement response is considered for selecting the force and deformation values to calculate the stiffness of the integrin molecule. The average stiffness of integrin models M1 (bare integrin), M2 (with Mn^{2+} ions) and M3 (with Mn^{2+} ions and ligand) are $2.19 \pm 0.28, 1.68 \pm 0.06$ and 1.53 ± 0.1 N/m, respectively. The stiffness of model M3 showed a lower value than other models in the pre-relaxation stiffening region, but as deformation continues, the model's behaviour is stiffer than models M2 and M1 in the post-relaxation stiffening region (figure 3*a*). The activation of model M3 during the equilibration promoted the unfolding of the integrin molecule in the pre-relaxation region. As a result, less force was required to pull the integrin molecule during the early stage of unfolding. Here, the activation of the integrin molecule was examined by measuring the hinge opening between the βA and the hybrid domain during equilibration [11,36]. To measure the hinge opening, we considered the bond distance between Asn^{303} from the βA domain and Lys^{417} from the Hybrid domain. After 2.4 ns of equilibration, the bond distance between selected residues for model M3 was permanently changed; but for other models, it stabilized at its original position (figure 4*a*). The permanent change in the bond distance caused the hinge opening for model M3. This demonstrates the activation of the integrin only for the M3 model (integrin attached to fibronectin) during equilibration. The presence of the Mn^{2+} ion in model M2 did not activate the integrin during the equilibration, as reported in past studies [12,27,37]. However, it influenced the behaviour of integrin in the initial stage of pulling (figure 3*a*). The effect of activation on the unfolding of integrin and deformational response is evaluated after analysing the breaking or formation of hydrogen bonds between different

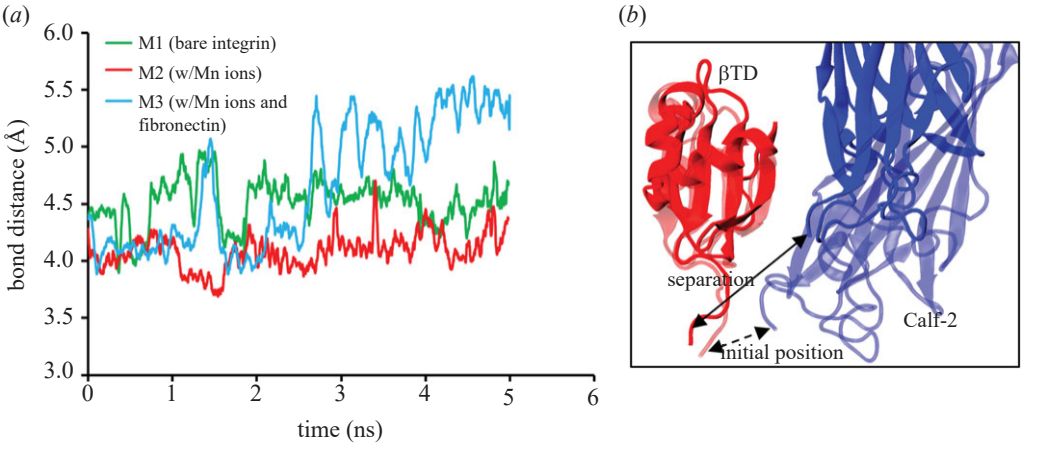

Figure 4. Structural changes at integrin headpiece and tailpiece region. (*a*) The hinge opening between the βA and the hybrid domains traced for bond distances between Asn^{308} and Lys^{417} for all integrin models during the equilibration. Only the IVB complex showed a permanent change in the bond distance by approximately 1.5 Å, indicating the activation of the IVB integrin structure. (*b*) Force-induced tensile deformation changed the interface between βTD and Calf-2 domains. The interfacial changes were observed between these domains at the initial state (Calf-2 (light blue) and βTD (light red)) and the separation at the final state (Calf-2 (blue) and βTD (red)).

domains. In figure 3*b*, the hydrogen bonds are counted between the head domains (hybrid and βA) and the tail domains (βTD, EGF-3 and EGF-4) to examine the separation of the tailpiece and headpiece domains. To elucidate the cause of more force exertion during the post-relaxation region, the hydrogen bonds in figure 3*c* are evaluated between the genu domains (Calf-1, and EGF-1, EGF-2). In figure 3*d*, the hydrogen bonds are analysed to capture the separation between tail domains (βTD and Calf-2). In these cases, because the evaluation of the hydrogen bonds between the selected domains was limited to fewer respective residues (the residues connected between the domains via hydrogen bonds) at the attachment site, the number of hydrogen bonds observed during the simulation varied in the 0–15 range. For the deactivated integrin, the head domains (hybrid and βA) and the tail domains (βTD, EGF-3 and EGF-4) of the subunit β_3 are attached (figure 1*a*). During tensile pulling, we observed the faster decrement of hydrogen bonds for model M3 compared to other models (figure 3*b*), leading to early detachment of the headpiece and tailpiece of the β_3 subunit and, thus, the activation of integrin. The faster detachment of head and tail domains reveals the role of integrin activation in the promotion of unfolding. The unfolding of integrin molecules results in less resistance to the applied force while pulling the integrin head.

A drastic reduction of hydrogen bonds occurs in all models around 20 Å and is accompanied by a reduction in the force on the integrin molecule for all the models. During this force relaxation, the integrin domains from the tail end (βTD and Calf-2) and at genu (Calf-1, EGF-1 and EGF-2) started the formation of hydrogen bonds. Figure 3*c* and *d* showed the formation of hydrogen bonds for tail-end domains (βTD and Calf-2) and domains at genu (Calf-1, EGF-1 and EGF-2) from the force relaxation region to the early part of the post-relaxation stiffening region (between 40 Å and 120 Å). These hydrogen bond formations increased the application of force during the unfolding of the integrin molecule in the post-relaxation stiffening region for all the models (figure 3*a*). The breaking of a hydrogen bond at the end of the post-relaxation stiffening region caused the separation of the interface between Calf-2 and the βTD domain (figure 4*b*). It reveals that the force-induced unfolding of integrin also contributes to the separation of tail domains (Calf-2 and βTD) for all models. Separation of tail domains has been observed during inside-out signalling [38]. The force-induced unfolding of integrin simulations suggests that integrin

activation leading to headpiece separation may contribute to tail domain separation, a potential outside-in signalling. Here we also observed an interesting deformational behaviour of model M3 in the post-relaxation stiffening region compared to the pre-relaxation stiffening region. A stiffer force response for model M3 than the other models is observed (figure 3*a*). During the pulling of model M3, the fibronectin ligand moved along with the integrin head. The deformation of the ligand exerted resistance to the unfolding of integrin, necessitating additional force for the movement of integrin. The prior experimental studies in literature also documented the stiffening behaviour of the ligand (fibronectin) binding integrin during unfolding [25,39]. A movie showing tensile deformation of integrin is shown in electronic supplementary material, document S2.

(b) Bending deformation of integrin in folding and unfolding direction

The cell traction force generated during cell migration [21] and fluid shear stress derived from interstitial fluid exerted the forced deformation in the integrin at the focal adhesion site [40]. Furthermore, the applied forces on integrin induced the tension in the cytoskeleton filament and regulated the gene expression by modulating protein complexes, which changed the morphology of the cell [40,41]. Bending simulations have been performed using constant velocity SMD for all integrin models to replicate such deformation in the integrin (figure 5*a*). The unfolded integrin structure (approx. 270 Å long) from tensile deformation for all the integrin models is used for the bending simulations. Here, the tail end of the integrin is fixed by constraining the centre of mass of selected atoms from the Calf-2 and βTD domains. Next, the βA and β-propeller domains at the head of the integrin are forced with constant velocity parallel to the tail end (figure 5*c*). The folding and unfolding directions of the integrin (figure 5*b*) are considered to investigate the bending deformation for all integrin models. The flexural rigidity of the integrin molecule has been evaluated after considering the integrin structure as a cantilever beam. It is calculated by using the given equation [42] $EI = Fl^3/3\delta$. Here, EI is expressed as flexural rigidity of component, where E and I are elastic Young's modulus and moment of inertia, respectively. The applied force (F) and deflection (δ) from the equation are obtained from the force-displacement plot for all integrin models. The maximum value of F and δ from the linear region of the force–displacement graph is used to estimate the flexural rigidity of the integrin molecule. The effective length (l) for EI calculation is determined from the deformed tensile integrin structure.

The flexural rigidity for all integrin models is tabulated in table 1 for folding and unfolding bending directions. The deformation directions for integrin molecules during the bending affected the flexural rigidity of all integrin models. A prior experimental study reported that molecular stiffness for integrin increases in the unfolding direction than folding direction as head-tail distance increases [25]. An increase in the bending stiffness leads to an increase in the flexural rigidity of the molecule ($EI\alpha(F/\delta)$). The present work using steered MD simulations confirmed that the flexural rigidity of all the integrin models increases in the unfolding direction compared to the folding direction (table 1). For the first time, based on our simulation results, we report the magnitudes of flexural modulus for the three integrin models. During the bending simulations of integrin in unfolded direction, the integrin molecule initially moved in the opposite direction of the application of force for all the models. The extended integrin molecules from tensile deformation used for the bending test tend to fold and retain their original folded shape. These extended integrin models mimic the behaviour of an unfolded bicycle kickstand touching the ground, where the position of the stand is restrained by the spring (figure 6*b*). Here, the tailpiece of the integrin can be thought of as a bicycle frame and the headpiece as a stand, and the induced force in the integrin that restrains the movement of the headpiece in the form of stored energy as a spring (figure 6*c*). As a result, when a force in the unfolding direction is applied, the headpiece of the integrin molecule moves initially in the folding direction until the applied forces overcome the induced forces in integrin; following which, the integrin moves in the unfolding direction (figure 6*a*). The induced forces in extended integrin molecules also influence the force responses for different velocities during bending in folding and unfolding directions. In the folding direction, the force generated for the maximum (0.03 Å/ps) velocity of pulling is less as compared

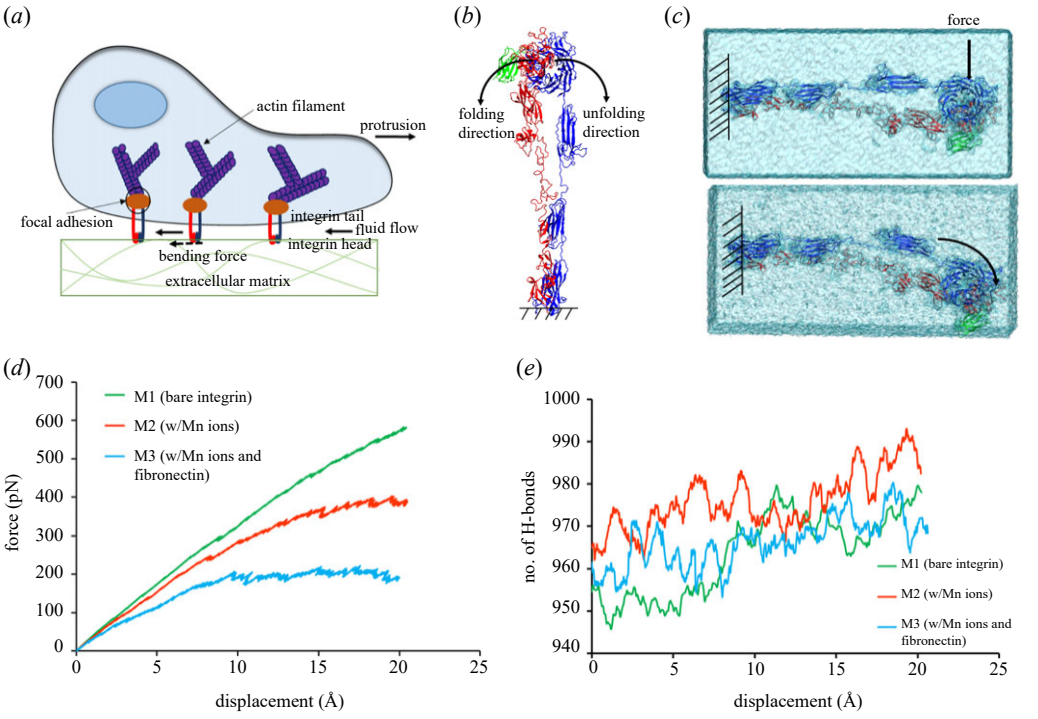

Figure 5. Schematic of the generation of bending loading on integrin and the bending deformation responses in the folding direction. (*a*) Illustration of the bending loading on integrin molecule due to the traction force from cell cytoskeleton and ECM, and interfacial fluid flow. (*b*) Representations of folding and unfolding directions of integrin structure during bending deformations. (*c*) Bending test set up and deformation of M3 showing constraints are applied at tail-end domain (Calf-2 and βTD), and head-end domains (βA and β-propeller) are forced for deformation in transverse direction. (*d*) The force–displacement responses of bending deformation in the folding direction showed the stiffer behaviour for M1 compared to M2 and M3. (*e*) The formation of a hydrogen bond at genu (Thigh and Calf-1 domain from α_v-subunit and EGF-1 and EGF-2 from β_3-subunit) indicates the rotation of head domains at the genu.

Table 1. Flexural rigidity of integrin models M1, M2 and M3 in folding and unfolding direction.

model	flexural rigidity in folding direction (N.m^2)	flexural rigidity in unfolding direction (N.m^2)
M1 (bare integrin)	$2.10 \times 10^{-26} \pm 0.04$	$3.76 \times 10^{-26} \pm 0.12$
M2 (w/Mn ions)	$1.7 \times 10^{-26} \pm 0.21$	$3.79 \times 10^{-26} \pm 0.01$
M3 (w/Mn ions + fibronectin)	$1.33 \times 10^{-26} \pm 0.02$	$4.3 \times 10^{-26} \pm 0.07$

to the minimum (0.01 Å/ps) velocity (electronic supplementary material, figure S1.6*a,b,c,e*). By contrast, this response reverses in the unfolding direction (electronic supplementary material, figure S1.7*a,c,e*). The stored energy in the integrin molecules favours the folding of integrin; thus, less force is required to bend the molecule in the folding direction.

We made an intriguing observation that as the models M2 and M3 bent in the unfolding direction, they showed a stiffer force response than the model M1 (figure 6*d*) and had larger magnitudes of flexural rigidity. It has been reported in the experimental literature that the interaction forces at the integrin-adhesion site changed with different ligand binding and the addition of various divalent cations in the integrin environment, leading to a change in integrin stiffness during unbending (unfolding) [25,27,30,37,43]. Here it was observed that for integrin

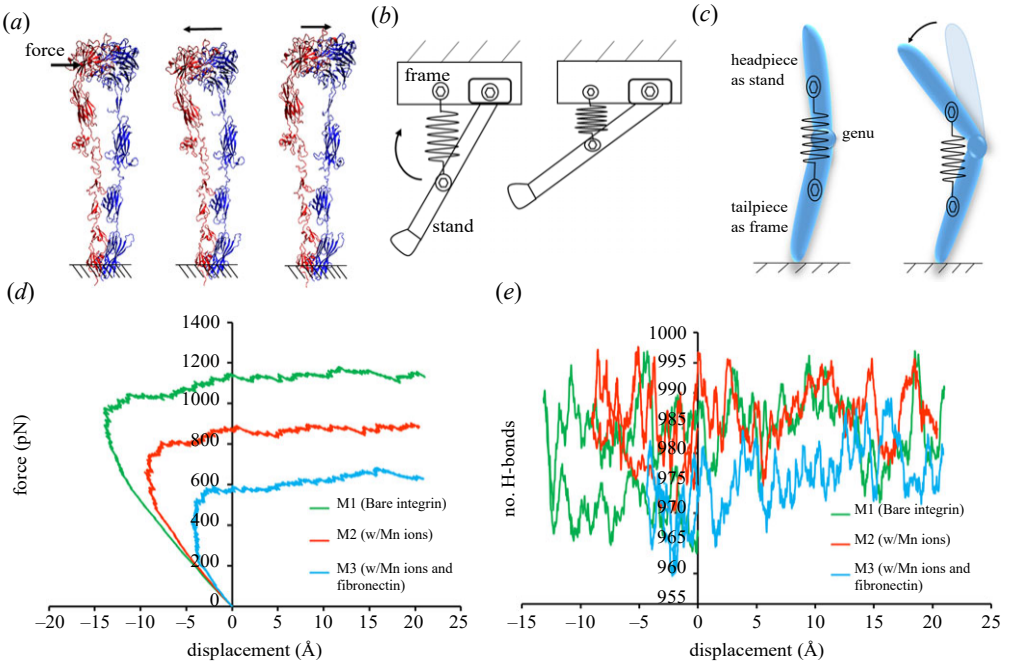

Figure 6. Bending deformation of integrin in unfolding direction. (*a*) Snapshots of representative bending deformation in the unfolding direction of M1 showed the deflection of the integrin headpiece opposite to the application of force at the initial phase of bending and then deformed in the direction of the force. (*b*) Schematic of bicycle kickstand where attached spring to the stand control the movement of the stand with frame. (*c*) Behaviour of the integrin molecule compared to the bicycle kickstand behaviour where induced force in the integrin as a spring controls the movement of the headpiece with tailpiece. (*d*) Force deformation response at 0.001 Å/ps velocity for all the models showed the negative displacement at initial bending indicates deflection of integrin in the folding direction against the application of force (*e*) increase in the hydrogen bonds at genu (Thigh and Calf-1 domain from α_V-subunit and EGF-1 and EGF-2 from β_3-subunit) as integrin start deflecting in unfolding direction.

in the presence of Mn^{2+} ion and fibronectin ligand, the flexural rigidity for models M2 and M3 changed with different integrin milieu as it bent in the unfolding direction **(**table 1**)**. As shown in figure 6*d*, due to prestressed condition, initially, the molecule moves in the folding direction until the preload is overcome and the molecule moves in the direction of loading. The preload for the three models is different and has magnitudes of 965.4 pN for M1, 699.9 pN for M2 and 432.3 pN for M3. However, the flexural rigidity of M3 is more than M2, which in turn is more than M1; thus, these values are affected by the preload. Also, when these preloads are overcome, the molecules continue to bend with little additional resistance. The force–displacement response in the folding direction (figure 5*d*), with model M1 requiring more force than models M2 and M3 for an equal amount of deflection, makes M1 more rigid than M2 and M3 (figure 6*d*). As stated in previous experimental studies in the literature, the addition of Mn^{2+} in the integrin environment and integrin-ligand ($FnIII_{10}$) binding altered the integrin activation and unfolding of the integrin structure [1,11,17,27,44].

During the bending simulations, it was observed that all the models were bent at 'genu' [45] for folding and unfolding directions (figures 5*c* and 6*a*). Hence, the bending deformation of integrin is analysed for H-bonds at the genu section for the Thigh and Calf-1 domain from α_V-subunit and EGF-1 and EGF-2 from β_3-subunit. Here in figures 5*e* and 6*e*, the hydrogen bonds are counted for all the selected domains at genu (Thigh and Calf-1 domain from α_V-subunit and EGF-1 and EGF-2 from β_3 -subunit), which include more residues from the selected domain to evaluate the hydrogen bonds and showed the higher hydrogen bonds magnitude during the

entire simulation. At genu, in the direction of folding, H-bond formation is observed (figure 5*e*), allowing the headpiece to deflect with less force. In the unfolding direction, the number of H-bonds decreases slightly for initial deflection and then starts the formation of bonds for all the integrin models. The deflection of integrin molecules in the folding direction is responsible for breaking the H-bonds at the initial phase; once the headpiece starts to move in the unfolding direction, the formation of H-bonds begins (figure 6*e*). The induced forces in the extended integrin structure and breaking of H-bonds caused the higher force for initial deflection at the beginning of bending in the unfolding direction (figure 6*d*). A movie showing the bending deformation of integrin in the folding direction is shown in electronic supplementary material, document S3. A movie showing the bending deformation of integrin in the unfolding direction is shown in electronic supplementary material, document S4.

3. Integrin molecule under torsion

Pulling cells from the attached ECM or substrate could twist the integrin structure at the adhesion site (figure 7*a*), where the applied forces from the cytoskeletal site and ECM would exert the torsional deformation in the integrin molecule. The integrin models have been investigated through a torsion loading path using SMD simulations to comprehend the behavioural changes in integrin under torsional deformation. Similar to the bending simulations, the extended integrin structures (approx. 270 Å long) from tensile deformation are used to conduct the torsion simulations for all the integrin models. To implement the torsional deformation in the integrin models, the tail end domains Calf-2 and βTD are fixed by applying the harmonic constraint, and the torque is applied at the head domains βA and β-propeller (figure 7*b*). Here, we employed the user-defined forced SMD to generate the toque at the headpiece of the integrin after applying angular acceleration on selected atoms (electronic supplementary material, document S1). The applied torque at the head side of the integrin creates the angular twist about the longitudinal axis of the integrin molecule. The responses of angular rotation to time are reported for three different angular accelerations. The torsional behaviour of the integrin molecule was evaluated for torsional stiffness and torsional rigidity, which is computed by using the given equation [42];

$$\text{Torsional stiffness} = \frac{T}{\vartheta}$$

and

$$\text{Torsional rigidity} = GJ = \frac{Tl}{\vartheta},$$

where T, ϑ, l, G and J are applied torque, angle of rotation (twist), length of the element, modulus of rigidity and polar moment of inertia, respectively. The extended integrin structure from tensile deformation determines the length (l) for torsional rigidity calculation. The maximum value for the angle of rotation (ϑ) is selected from the linear regime to calculate the stiffness and rigidity. The torsional properties of all integrin models are evaluated for the first linear regime from the angle displacement plot. After implementing the torque on the molecule, the alterations in the integrin structure cause a change in the behaviour of the rotation plot.

The angle of twist for all integrin models plotted for different angular accelerations shows the increment in angular displacement as angular acceleration (torque) increases for the selected time (figure 7*d*). The change in behaviour in the angle of rotation plot has been observed for angular acceleration of 0.03 rad/ps^2 in all integrin models (electronic supplementary material, figure S1.8*a,c,e*). Hence these plots are considered for evaluating the torsional properties of integrin molecules. The change in behaviour in angular displacement for models M2 and M3 is observed at a smaller angle than in model M1 (figure 7*d*). It is measured as 105, 100 and 98 degrees for models M1, M2 and M3, respectively. Torsional stiffness and torsional rigidity of all integrin models for the measured angle of rotation and applied torque are computed and shown in table 2. In past experimental studies in the literature, it was shown that the integrin molecule became stiffer in the presence of Mn^{2+} ions and ligand as the cell was forced to move [25,43]. Here, the effect of

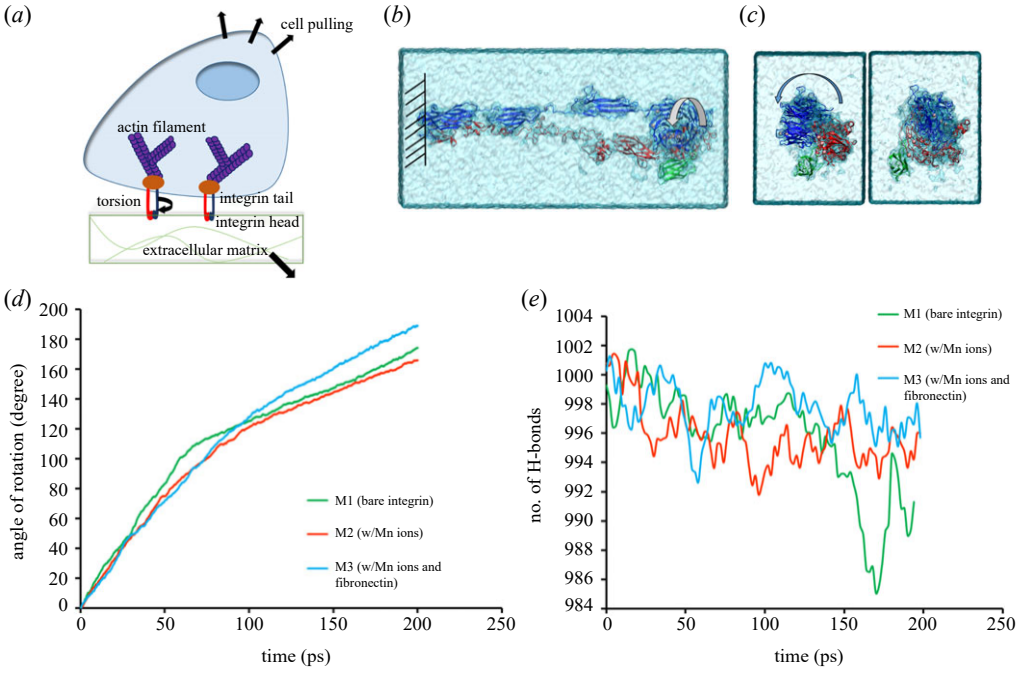

Figure 7. Graphical representation of formation torsion on integrin molecule, torsion test set-up and torsional deformation response (*a*) schematic illustrates twisting of integrin structure as cell, and ECM deformed in the opposite direction. (*b*) For torsion test set-up, the tail end domains (Calf-2 and βTD) are fixed and the angular acceleration applied at head domains (βA and β-propeller) of the integrin. (*c*) The initial and final state of integrin molecule along the longitudinal axis showed the dense integrin structure in the centre of rotational axis. (*d*) Angular displacement response of all integrin models at 0.003 rad/ps^2 showed softening behaviour for M1 as compared to M2 and M3 (*e*) The rotation of integrin caused the decrement in the hydrogen bonds at head domains.

Table 2. Torsional stiffness and torsional rigidity for integrin models M1, M2 and M3.

model	torsional stiffness (N.m)	torsional rigidity (N.m^2)
M1 (bare integrin)	$5.88 \times 10^{-19} \pm 0.15$	$1.59 \times 10^{-26} \pm 0.04$
M2 (w/Mn ions)	$6.31 \times 10^{-19} \pm 0.26$	$1.7 \times 10^{-26} \pm 0.07$
M3 (w/Mn ions + fibronectin)	$6.43 \times 10^{-19} \pm 0.28$	$1.73 \times 10^{-26} \pm 0.07$

torsion is considered based on the application of force from the extracellular side and cell pulling. As a result, model M2 and M3 exhibited more torsional rigidity than model M1 (table 2). Model M3 showed resistance in the early stage of torsion compared to other models. As the integrin molecule dissociated from the ligand from its ligand binding side after 100 ps, it changed its behaviour and rotated faster than other models (figure 7*d*).

The structure in the centre of the integrin molecule along the longitudinal axis became denser as the molecule started rotating, exerting more resistance to the rotation of integrin (figure 7*c*). Therefore, to understand this torsional behaviour, all integrin models are investigated for H-bonds analysis between head domains of integrin βA and β-propeller. For all models, the breaking of H-bonds is more pronounced in the initial stages of rotation (approx. up to 70 ps); however, as the integrin structure gets denser at the centre, the breaking of H-bonds at the head domains of the integrin decreases (figure 7*e*). The decrement in the breaking of H-Bonds resulted in resisting the molecule's rotation, causing a change in the slope of the curve for the angle of

rotation versus the time plot (figure 7*d*). As a result, here we confirmed that the different integrin environments influence the torsional behaviour of the integrin molecule along with its structural changes during torsion. A movie showing torsional deformation of integrin is shown in electronic supplementary material, document S5.

4. Conclusion

In the present work, the SMD simulations were performed to investigate the mechanical response of the integrin for different integrin milieus under various loading conditions. The significant impact of Mn^{2+} ion and ligand binding was found on the integrin behaviour under various loading paths. Under tensile loading, we observed different deformation behaviour for ligand (fibronectin) binding integrin during the initial pulling and after force relaxation. The ligand binding activated the integrin and influenced the unfolding of the integrin molecule after fast-detaching the headpiece and tailpiece domains during initial pulling. The fast detachment in head and tail domains induced less force in the integrin molecule, resulting in lower stiffness for the ligand binding integrin molecule. However, the deformation behaviour for partially open ligand binding integrin changed and became stiffer as compared to unliganded integrin molecules. The bound ligand resisted the force-induced switchblade motion in integrin, increasing the force for the deformation.

Further, we observed the bending and torsional deformation for the extended integrin molecules after the tensile deformation. It appears that the unfolding of the integrin results in a prestress condition that causes refolding of the integrin upon release of applied force. This profoundly impacts the bending response of the integrin molecule and causes the flexural stiffness to be dependent on the direction of loading. The flexural stiffness of the integrin molecule is less in the folding direction than in the unfolding direction. We have evaluated the prestress loads for all models. Due to the prestressed structure, it makes the bending easy in the folding direction but provides resistance for the unfolding motion of the integrin. Also, the integrin molecule with Mn^{2+} ion and ligand bent more easily in the folding direction than bare integrin, but in the unfolding direction, these molecules became stiffer. Further, we found that the presence of Mn^{2+} and ligand has also influenced the torsional properties of integrin during torsional deformation. However, no significant difference has been observed in torsional properties between ligand-bound integrin and integrin molecules in the presence of Mn^{2+}. For the first time, based on our simulation results, we report the magnitudes of tensile modulus, flexural stiffness and torsional stiffness for the three different integrin environments. The force-induced unfolding of integrin simulations suggests that integrin activation leading to headpiece separation and contributes to tail domain separation, a potential outside-in signalling. The presented study provides valuable insights and a plausible explanation for defining the mechanics of integrin for different environments and describes the mechanical response of integrin to various loading conditions. The results from this work would be essential for the development of accurate multiscale models of cellular adhesion and migration, which is integral to many physiological and pathological conditions.

5. Material and methods

(a) Integrin model set-up and molecular dynamics simulations:

In this study, the fibronectin-binding integrin $\alpha_v\beta_3$ protein structure (PDB code 4MMX) [17] has been used for the simulations. This protein structure consists of α_v and β_3 subunits, Mn^{2+} ions, the tenth type III RGD domain of fibronectin ($FnIII_{10}$ ligand), and carbohydrates. Here to analyse the effect of divalent cation and ligand binding on integrin properties, three integrin models were prepared from $\alpha_v\beta_3$ protein structure. First, the original protein structure is used as model M3. Next, model M2 was created after removing the ligand from the original structure. Then the ligand and Mn^{2+} ions were removed from the original protein structure to prepare

model M1. For prepared models, using topology and parameter files from Harvard molecular mechanics (CHARMM) [46], the protein structure and coordinate files were generated in visual molecular dynamics (VMD) software [47]. Nanoscale molecular dynamics (NAMD) psfgen tool [48] was used to generate these files in VMD. Next, the TIP3P force field was used with the VMD plugin to prepare a solvated structure of the integrin molecule in a water box where the distance between the water box walls and the proteins was set to 10 Å. Then, the system was brought to electrostatic neutrality using the VMD autoionize feature. All MD simulations were performed using the NAMD [49] software and the CHARMM36 force fields [50]. We used 0.5 fs timestep and considered 12 Å cut-off and 10 Å switching distance for all non-bonded interactions. Initially, the energy minimization of the molecule is carried out by the conjugate gradient method. Then, the temperature and the pressure of the molecule were increased to 300 K and 1.01325 bar, respectively, in incremental steps of 50 K and 0.25 bar. Next, the equilibrium simulation of the integrin models was carried out for 5 ns in the NPT ensemble condition (isobaric-isothermal). Langevin dynamics and Nose–Hoover piston methods were adopted to control temperature and pressure during simulation [51,52]. To implement particle Mesh Ewald (PME) electrostatic interactions, molecular dynamic simulations of the integrin models were performed with periodic boundary conditions. All the equilibrated integrin models were verified for equilibrium state through the root mean squared deviation data and then used for SMD simulations.

(b) Steered molecular dynamics simulations

SMD is an extended MD simulation method for studying the force-induced response of molecules that mimics the fundamental concepts of atomic force microscopy (AFM) and offers a unique atom-by-atom dynamical perspective of molecular mechanical response [53]. SMD has two standard protocols: constant force (loading-based) and constant velocity pulling (deformation-based). In constant force SMD, a constant force is directly applied to a specific atom or a group of atoms, and displacement is monitored throughout dynamics. In constant velocity SMD, a harmonic potential (a virtual spring) is attached between a specific atom or group of atoms and dummy atoms, and this dummy atom is moved at constant velocity in a chosen direction while the SMD atoms attached to the other end of the spring are subject to the steering force and monitored for the entire simulation. In many cases, the constant velocity SMD overestimates force values due to usually applied high velocities values. Because of limitations in computational resources, even the slowest stretching velocities used in simulations are higher in magnitude than those used in equivalent AFM experiments [54]. From the computational point of view, the coarse-grained (CG) MD approach [55] and atoms-to-beam homogenization approach [56] are reported as the most promising approaches to predict structural features while achieving computational efficiency, i.e. lowering production times. However, the coarse-grained (CG) MD approach has limited monitoring of non-covalent interactions interplay, such as H-bond formation and breakage, while the atoms-to-beam homogenization approach still relies on the validation through experimental characterization [57,58]. Nevertheless, the constant velocity SMD approach may still qualitatively reproduce force profiles from a single molecule force spectroscopy [59]. The constant force SMD can be used to compare the relative strengths of major unfolding processes and evaluate the solvent interactions; however, selecting the appropriate applied force values requires prior system knowledge. Furthermore, high force value may hamper observation of unfolding events, while low values would not be sufficient to overcome barriers [60].

In this study, the tension and bending simulations were performed using the NAMD implemented constant velocity pulling approach [49]. For the tensile simulations, the β tail domain (βTD) of the β_3 subunit was fixed, and βA and β-propeller domains from the integrin headpiece were pulled with constant velocity. Here α carbon atoms of some residues from these domains were selected, then the force and constraint were exerted on the centre of mass (COM) of the selected atoms. The selected residues for pulled or constraint domains are as follows: βA

residues 113–117, 151–156, 244–250,306–310, 329–332; β-propeller residues 97–101, 1260–132, 160–164, 225–229, 279–283, 343–347, 407–411and βTD residues 610–620, 639–642, 656–658, 665–670. The pulling COM of the selected domains was harmonically constrained with the spring constant. The optimum spring constant for COM was determined by performing tension test simulations for various spring constant values (refer to electronic supplementary material, document S1.1). Based on the results, a spring constant of 3 kcal/mol/Å^2 was chosen. The deformation-controlled tension was applied for 0.01, 0.02, 0.03, 0.04 and 0.05 Å/ps velocities, where minimum velocity was selected after referring to previous studies [31,32]. The extended integrin structure (approx. 270 Å long) for all models was used for performing bending and torsion simulations. The bending test simulation was performed by constraining the tail-end and pulling the head-end of integrin in a transverse direction. Residues from the Calf-2 domain were fixed in the bending simulation in addition to the residues chosen for the tension simulation. The same residues of the head domains from the tension simulations were used for pulling in the bending simulation. The selected residues of the Calf-2 domain are 940–952 and 919–930. The constant velocities used in bending test simulations were 0.01, 0.02 and 0.03 Å/ps. The torsion test was performed using user-defined forces in the SMD simulation. During torsion simulations, the same residues from the bending simulations were used, the tail-end of the integrin was fixed, and different angular accelerations were applied to the head-end of the integrin. The angular accelerations used for simulations were 0.01, 0.02 and 0.03 rad/ps^2. The simulation was repeated three times to evaluate the mechanical properties of integrin models. All the presented graphs and calculated mechanical properties came from averaging the outcomes of all simulations. For all simulations, the hydrogen bond was defined using a combination of geometric parameters (donor hydrogen distance < 3.5 Å and 120° ≤ donor-hydrogen-acceptor angle). The integrin $\alpha_v\beta_3$ domains are defined as follows: β-propeller residues 1–438; Thigh domain residues 439–600; Calf1 residues 601–738; Calf-2 residues 739–956; PSI residues 1–57; hybrid domain residues 58–110 and 354 to 434; βA residues 111–353; EGF-1 residues 435–472; EGF-2 residues 473–522; EGF-3 residues 523–559; EGF-4 residues 560–605 and the β tail domain (βTD) residues 606–690. VMD was employed to render the images, analyse the geometry and generate the videos.

Data accessibility. The data are provided in electronic supplementary material [61].

Authors' contributions. H.K.G.: formal analysis, investigation, validation, visualization, writing—original draft; S.V.J.: formal analysis, investigation, validation, visualization, writing—original draft; K.S.K.: conceptualization, funding acquisition, project administration, supervision; A.H.: methodology, writing—review and editing; D.R.K.: conceptualization, data curation, funding acquisition, investigation, methodology, project administration, resources, software, supervision, validation, visualization, writing—review and editing.

All authors gave final approval for publication and agreed to be held accountable for the work performed therein.

Conflict of interest declaration. We declare we have no competing interests.

Funding. National Science Foundation supported this work under NSF EPSCoR Track-1 Cooperative Agreement OIA no. 1946202. NSF grant nos 1229316 and 2019077 are acknowledged for the support of the computational resources at NDSU CCAST.

References

1. Hynes RO. 2002 Integrins: bidirectional, allosteric signaling machines. *Cell* **110**, 673–687. (doi:10.1016/S0092-8674(02)00971-6)
2. Haage A *et al.* 2020 Precise coordination of cell-ECM adhesion is essential for efficient melanoblast migration during development. *Development* **147**, dev184234. (doi:10.1242/dev.184234)
3. Humphries MJ. 1990 The molecular basis and specificity of integrin-ligand interactions. *J. Cell Sci.* **97**, 585–592. (doi:10.1242/jcs.97.4.585)
4. van der Flier A, Sonnenberg A. 2001 Function and interactions of integrins. *Cell Tissue Res.* **305**, 285–298. (doi:10.1007/s004410100417)

5. Arnaout MA, Goodman SL, Xiong JP. 2007 Structure and mechanics of integrin-based cell adhesion. *Curr. Opin Cell Biol.* **19**, 495–507. (doi:10.1016/j.ceb.2007.08.002)
6. Anderson LR, Owens TW, Naylor MJ. 2014 Structural and mechanical functions of integrins. *Biophys. Rev.* **6**, 203–213. (doi:10.1007/s12551-013-0124-0)
7. Schiller HB *et al.* 2013 β1- and αv-class integrins cooperate to regulate myosin II during rigidity sensing of fibronectin-based microenvironments. *Nat. Cell Biol.* **15**, 625–636. (doi:10.1038/ncb2747)
8. Kulke M, Langel W. 2020 Molecular dynamics simulations to the bidirectional adhesion signaling pathway of integrin αVβ3. Proteins: structure. *Funct. Bioinform.* **88**, 679–688. (doi:10.1002/prot.25849)
9. Xiao T, Takagi J, Coller BS, Wang J-H, Springer TA. 2004 Structural basis for allostery in integrins and binding to fibrinogen-mimetic therapeutics. *Nature* **432**, 59–67. (doi:10.1038/nature02976)
10. Takagi J, Springer TA. 2002 Integrin activation and structural rearrangement. *Immunol. Rev.* **186**, 141–163. (doi:10.1034/j.1600-065X.2002.18613.x)
11. Takagi J, Petre BM, Walz T, Springer TA. 2002 Global conformational rearrangements in integrin extracellular domains in outside-in and inside-out signaling. *Cell* **110**, 599–611. (doi:10.1016/S0092-8674(02)00935-2)
12. Mould AP *et al.* 2003 Conformational changes in the integrin αIA domain provide a mechanism for signal transduction via hybrid domain movement. *J. Biol. Chem.* **278**, 17 028–17 035. (doi:10.1074/jbc.M213139200)
13. Luo B-H, Springer TA, Takagi J. 2003 Stabilizing the open conformation of the integrin headpiece with a glycan wedge increases affinity for ligand. *Proc. Natl Acad. Sci. USA* **100**, 2403–2408. (doi:10.1073/pnas.0438060100)
14. Vinogradova O *et al.* 2002 A structural mechanism of integrin αIIbβ3 'inside-out' activation as regulated by its cytoplasmic face. *Cell* **110**, 587–597. (doi:10.1016/S0092-8674(02)00906-6)
15. Bidone TC, Skeeters AV, Oakes PW, Voth GA. 2019 Multiscale model of integrin adhesion assembly. *PLoS Comput. Biol.* **15**, e1007077. (doi:10.1371/journal.pcbi.1007077)
16. Friedland JC, Lee MH, Boettiger D. 2009 Mechanically activated integrin switch controls α5β1 function. *Science* **323**, 642. (doi:10.1126/science.1168441)
17. Van Agthoven JF *et al.* 2014 Structural basis for pure antagonism of integrin α V β 3 by a high-affinity form of fibronectin. *Nat. Struct. Mol. Biol.* **21**, 383–388. (doi:10.1038/nsmb.2797)
18. Liu Z, Wang F, Chen X. 2008 Integrin αvβ3-targeted cancer therapy. *Drug Dev. Res.* **69**, 329–339. (doi:10.1002/ddr.20265)
19. Guo W, Giancotti FG. 2004 Integrin signalling during tumour progression. *Nat. Rev. Mol. Cell Biol.* **5**, 816–826. (doi:10.1038/nrm1490)
20. Pan B, Guo J, Liao Q, Zhao Y. 2018 β1 and β3 integrins in breast, prostate and pancreatic cancer: a novel implication. *Oncol. Lett.* **15**, 5412–5416. (doi:10.3892/ol.2018.8076)
21. Baker EL, Zaman MH. 2010 The biomechanical integrin. *J. Biomech.* **43**, 38–44. (doi:10.1016/j.jbiomech.2009.09.007)
22. Chang AC, Mekhdjian AH, Morimatsu M, Denisin AK, Pruitt BL, Dunn AR. 2016 Single molecule force measurements in living cells reveal a minimally tensioned integrin state. *ACS Nano* **10**, 10 745–10 752. (doi:10.1021/acsnano.6b03314)
23. Litvinov RI, Shuman H, Bennett JS, Weisel JW. 2002 Binding strength and activation state of single fibrinogen-integrin pairs on living cells. *Proc. Natl Acad. Sci. USA* **99**, 7426–7431. (doi:10.1073/pnas.112194999)
24. Harjumäki R *et al.* 2020 AFM force spectroscopy reveals the role of integrins and their activation in cell–biomaterial interactions. *ACS Appl. Bio Mater.* **3**, 1406–1417. (doi:10.1021/acsabm.9b01073)
25. Chen Y, Lee H, Tong H, Schwartz M, Zhu C. 2017 Force regulated conformational change of integrin αVβ3. *Matrix. Biol.* **60**, 70–85. (doi:10.1016/j.matbio.2016.07.002)
26. Sun Z *et al.* 2005 Mechanical properties of the interaction between fibronectin and α5β1-integrin on vascular smooth muscle cells studied using atomic force microscopy. *Am. J. Physiol. Heart Circ. Physiol.* **289**, H2526–H2535. (doi:10.1152/ajpheart.00658.2004)
27. Bachmann M *et al.* 2020 Induction of ligand promiscuity of αVβ3 integrin by mechanical force. *J. Cell Sci.* **133**, jcs242404. (doi:10.1242/jcs.242404)

28. Dickeson SK, Walsh JJ, Santoro SA. 1997 Contributions of the I and EF hand domains to the divalent cation-dependent collagen binding activity of the α2β1 integrin. *J. Biol. Chem.* **272**, 7661–7668. (doi:10.1074/jbc.272.12.7661)
29. D'Souza SE *et al.* 1994 Ligand and cation binding are dual functions of a discrete segment of the integrin β3 subunit: cation displacement is involved in ligand binding. *Cell* **79**, 659–667. (doi:10.1016/0092-8674(94)90551-7)
30. Plow EF, Haas TA, Zhang L, Loftus J, Smith JW. 2000 Ligand binding to integrins. *J. Biol. Chem.* **275**, 21 785–2 1788. (doi:10.1074/jbc.R000003200)
31. Puklin-Faucher E, Gao M, Schulten K, Vogel V. 2006 How the headpiece hinge angle is opened: new insights into the dynamics of integrin activation. *J. Cell Biol.* **175**, 349–360. (doi:10.1083/jcb.200602071)
32. Chen W, Lou J, Hsin J, Schulten K, Harvey SC, Zhu C. 2011 Molecular dynamics simulations of forced unbending of integrin αVβ3. *PLoS Comput. Biol.* **7**, e1001086. (doi:10.1371/journal.pcbi.1001086)
33. Zhu J, Luo B-H, Xiao T, Zhang C, Nishida N, Springer TA. 2008 Structure of a complete integrin ectodomain in a physiologic resting state and activation and deactivation by applied forces. *Mol. Cell* **32**, 849–861. (doi:10.1016/j.molcel.2008.11.018)
34. Jaswandkar SV, Faisal HMN, Katti KS, Katti DR. 2021 Dissociation mechanisms of G-actin subunits govern deformation response of actin filament. *Biomacromolecules* **22**, 907–917. (doi:10.1021/acs.biomac.0c01602)
35. Pradhan SM, Katti DR, Katti KS. 2011 Steered molecular dynamics study of mechanical response of full length and short collagen molecules. *J. Nanomec. Micromech.* **1**, 104–110. (doi:10.1061/(ASCE)NM.2153-5477.0000035)
36. Wriggers W, Schulten K. 1997 Protein domain movements: detection of rigid domains and visualization of hinges in comparisons of atomic coordinates. *Proteins Struct. Funct. Bioinform.* **29**, 1–14. (doi:10.1002/(SICI)1097-0134(199709)29:1<1::AID-PROT1>3.0.CO;2-J)
37. Zhu J, Zhu J, Springer TA. 2013 Complete integrin headpiece opening in eight steps. *J. Cell Biol.* **201**, 1053–1068. (doi:10.1083/jcb.201212037)
38. Anthis NJ, Campbell ID. 2011 The tail of integrin activation. *Trends Biochem. Sci.* **36**, 191–198. (doi:10.1016/j.tibs.2010.11.002)
39. Li F, Redick SD, Erickson HP, Moy VT. 2003 Force measurements of the α5β1 integrin–fibronectin interaction. *Biophys. J.* **84**, 1252–1262. (doi:10.1016/S0006-3495(03)74940-6)
40. Jasuja HA-O, Kar SA-O, Katti DA-O, Katti KA-O. 2021 Perfusion bioreactor enabled fluid-derived shear stress conditions for novel bone metastatic prostate cancer testbed. *Biofabrication* **13**, 035004. (doi:10.1088/1758-5090/abd9d6)
41. Chicurel ME, Singer RH, Meyer CJ, Ingber DE. 1998 Integrin binding and mechanical tension induce movement of mRNA and ribosomes to focal adhesions. *Nature* **392**, 730–733. (doi:10.1038/33719)
42. Gere JM, Goodno BJ. 2012 *Mechanics of materials: Cengage lear*ning.
43. Lange JR, Goldmann WH, Alonso JL. 2016 Influence of αvβ3 integrin on the mechanical properties and the morphology of M21 and K562 cells. *Biochem. Biophys. Res. Commun.* **478**, 1280–1285. (doi:10.1016/j.bbrc.2016.08.111)
44. Cluzel C, Fdr S, Lussi J, Fdr P, Imhof BA, Wehrle-Haller B. 2005 The mechanisms and dynamics of αvβ3 integrin clustering in living cells. *J. Cell Biol.* **171**, 383–392. (doi:10.1083/jcb.200503017)
45. Xiong J-P *et al.* 2001 Crystal structure of the extracellular segment of integrin αVβ3. *Science* **294**, 339–345. (doi:10.1126/science.1064535)
46. MacKerell Jr AD *et al.* 1998 All-atom empirical potential for molecular modeling and dynamics studies of proteins. *J. Phys. Chem. B* **102**, 3586–3616. (doi:10.1021/jp973084f)
47. Humphrey W, Dalke A, Schulten K. 1996 VMD: visual molecular dynamics. *J. Mol. Grap.* **14**, 33–38. (doi:10.1021/jp973084f)
48. Nelson MT *et al.* 1996 NAMD: a parallel, object-oriented molecular dynamics program. *Int. J. Supercomputer Appl. High Perform. Comput.* **10**, 251–268. (doi:10.1177/109434209601000401)
49. Phillips JC *et al.* 2005 Scalable molecular dynamics with NAMD. *J. Comput. Chem.* **26**, 1781–1802. (doi:10.1002/jcc.20289)
50. Brooks B, Karplus M. 1983 Harmonic dynamics of proteins: normal modes and fluctuations in bovine pancreatic trypsin inhibitor. *Proc. Natl Acad. Sci. USA* **80**, 6571–6575. (doi:10.1073/pnas.80.21.6571)

51. Zhang Y, Feller SE, Brooks BR, Pastor RW. 1995 Computer simulation of liquid/liquid interfaces. I. Theory and application to octane/water. *J. Chem. Phys.* **103**, 10 252–10 266. (doi:10.1063/1.469927)
52. Martyna GJ, Tobias DJ, Klein ML. 1994 Constant pressure molecular dynamics algorithms. *J. Chem. Phys.* **101**, 4177–4189. (doi:10.1063/1.467468)
53. Grubmüller H. 2005 Force probe molecular dynamics simulations. *Protein Ligand Interact.*, 493–515. (doi:10.1385/1-59259-912-5_493)
54. Gao M, Sotomayor M, Villa E, Lee EH, Schulten K. 2006 Molecular mechanisms of cellular mechanics. *Phys. Chem. Chem. Phys.* **8**, 3692–3706. (doi:10.1039/B606019F)
55. Kmiecik S, Wabik J, Kolinski M, Kouza M, Kolinski A. 2014 Coarse-grained modeling of protein dynamics. In *Computational methods to study the structure and dynamics of biomolecules and biomolecular processes*, pp. 55–79. Berlin, Germany: Springer.
56. Kalliauer J, Kahl G, Scheiner S, Hellmich C. 2020 A new approach to the mechanics of DNA: atoms-to-beam homogenization. *J. Mech. Phys. Solids* **143**, 104040. (doi:10.1016/j.jmps.2020.104040)
57. Kim Y-J, Kim D-N. 2016 Structural basis for elastic mechanical properties of the DNA double helix. *PLoS ONE* **11**, e0153228. (doi:10.1371/journal.pone.0153228)
58. Lu H, Isralewitz B, Krammer A, Vogel V, Schulten K. 1998 Unfolding of Titin immunoglobulin domains by steered molecular dynamics simulation. *Biophys. J.* **75**, 662–671. (doi:10.1016/S0006-3495(98)77556-3)
59. Lu H, Schulten K. 2000 The key event in force-induced unfolding of titin's immunoglobulin domains. *Biophys. J.* **79**, 51–65. (doi:10.1016/S0006-3495(00)76273-4)
60. Isralewitz B, Baudry J, Gullingsrud J, Kosztin D, Schulten K. 2001 Steered molecular dynamics investigations of protein function. *J. Mol. Graphics Modell.* **19**, 13–25. (doi:10.1016/s1093-3263(00)00133-9)
61. Gaikwad HK, Jaswandkar SV, Katti KS, Haage A, Katti DR. 2023 Molecular basis of conformational changes and mechanics of integrins. Figshare. (doi:10.6084/m9.figshare.c.6494013)